Lin et al. *Microsystems & Nanoengineering* (2026)12:89
https://doi.org/10.1038/s41378-026-01184-6

Microsystems & Nanoengineering
www.nature.com/micronano

ARTICLE Open Access

Boron-doped diamond solution-gate field-effect transistor (BDD-SGFET) biosensor for gene mutation detection

Zelong Lin[1,2,3,4], Yun Zheng[1,2,3,4], Yisen Chen[1,2,3,4], Chengyong Wang[1,2,3,4] and Zhishan Yuan[1,2,3,4]✉

Abstract

Gene mutation is one of the core pathogenic factors in numerous major diseases, making the detection of base mismatches resulting from these mutations critically important in both biological and clinical contexts. This study presents a high-performance boron-doped diamond solution-gated field-effect transistor (BDD-SGFET) biosensor, designed with a diamond microwire structure, for the label-free detection of base mismatches associated with EGFR gene mutations. The simulations examining the impact of variations in diamond microwire dimensions on the electrical properties of BDD-SGFET reveal that increasing the microwire width while reducing its length enhances the electrical performance of the device. Utilizing microwave plasma chemical vapor deposition (MPCVD), photolithography, and plasma etching, we successfully fabricated high-performance BDD-SGFETs featuring microwire structures that demonstrate outstanding transconductance, a reduced threshold voltage, and a limit of detection of 10 pM. Notably, the enhanced performance of the fabricated BDD-SGFET enables the successful identification of DNA molecules with two base-pair mismatches. Furthermore, the device exhibits impressive anti-interference capabilities and exceptional stability in complex environments. These findings highlight the significant potential of microscale BDD-SGFETs as rapid, label-free, and robust platforms for point-of-care testing in genetic mutation analysis pertinent to cancer diagnosis.

Introduction

Gene mutation represents one of the key pathogenic factors in numerous major diseases, including cystic fibrosis, thalassemia, and sickle cell disease[1]. Base mismatching acts as a fundamental molecular event that arises from DNA replication errors[2], damage[3], or genetic variation[4]. Consequently, the detection of base mismatches holds paramount biological and clinical significance. Primarily, maintaining the fidelity of genetic information is critical for cellular function and organismal viability. Unrepaired base mismatches can result in permanent mutations that are transmitted to daughter cells[5], contributing to increased genomic instability. Additionally, base mismatches are a significant source of somatic mutations and are strongly associated with the onset of various cancers, including non-small cell lung cancer (NSCLC)[6], along with numerous genetic disorders[7]. Furthermore, efficient mismatch detection and repair mechanisms protect cells from endogenous damage[8]. In biotechnological applications, accurate DNA sequences are essential for procedures such as PCR, gene cloning, and gene editing[9]. Therefore, technologies that enable precise detection of base mismatches are crucial for understanding diseases, facilitating early diagnosis, guiding therapies, and ensuring quality control[10].

In the context of mutant gene detection, sequencing technologies such as Sanger sequencing[11] and amplification-based methodologies like quantitative real-time PCR (qRT-PCR)[12] are regarded as gold standards due to their high accuracy and reliability, whereas digital

Correspondence: Zhishan Yuan (zhishanyuan@gdut.edu.cn)
[1]School of Electro-Mechanical Engineering, Guangdong University of Technology, Guangzhou, China
[2]Guangdong Provincial Key Laboratory of Minimally Invasive Surgical Instruments and Manufacturing Technology, Guangdong University of Technology, Guangzhou, China
Full list of author information is available at the end of the article
These authors contributed equally: Zelong Lin, Yun Zheng, Yisen Chen

PCR is recognized for its remarkable sensitivity. However, the implementation of these technologies is often hindered by extensive sample preprocessing, dependence on nucleic acid amplification, and the necessity for sophisticated optical detection systems, which limit their effectiveness in point-of-care (POC) testing and home healthcare environments[13]. Optical and electrochemical biosensing techniques have emerged as promising alternatives to address these challenges. While optical methods provide high sensitivity, they frequently require costly labeling agents, intricate optical instrumentation, and labor-intensive sample preparation, rendering them less suitable for low-cost, portable, and rapid diagnostics[14]. Conversely, electrochemical platforms, though more compact and simpler in instrumentation, face substantial challenges, including susceptibility to matrix interference in complex biological samples, limited sensitivity, and inadequate anti-fouling properties, which impede their capability to detect low-abundance mutations with high specificity[15].

Field-effect transistor (FET) biosensors have emerged as a cornerstone technology for next-generation molecular diagnostics, owing to their label-free detection, high sensitivity, real-time response, and compatibility with microelectronic fabrication processes that facilitate miniaturization and system integration[16]. The sensing mechanism is essentially based on the modulation of channel conductance through charge variations generated when target molecules (such as EGFR gene fragments) hybridize with immobilized probes on the gate surface, enabling direct electrical signal transduction[17].

Traditional FET sensors are primarily fabricated using semiconductor materials such as silicon (Si) and metal oxides like indium tin oxide (ITO)[18]. Despite advancements in silicon-based FET sensors (including ISFET[19] and SiNW-FET[20]), these devices are susceptible to surface oxidation and corrosion in extreme pH or electrolytic environments, resulting in inadequate long-term stability. In contrast, metal oxides such as ITO exhibit brittleness, limited flexibility, and biocompatibility[21]. Additionally, these materials produce substantial background currents within their electrochemical windows during operation. Upon the application of a detection potential, the materials undergo redox reactions, generating substantial noise that obscures weak specific signals[22], thereby compromising the signal-to-noise ratio and elevating the limit of detection[23].

Boron-doped p-type conductive diamond is emerging as a highly attractive material in the field of electronic devices[24]. Diamond mainly features the widest electrochemical window among known materials (approximately 3.5 V), which effectively mitigates background currents[25]. Additionally, diamond offers remarkable physical and chemical stability[26], superior biocompatibility[27], and ease of surface functionalization[28]. These attributes position diamond as an ideal channel material for FETs, facilitating the detection of a variety of biomolecules, including ions, antigen-antibody complexes, and DNA, due to its excellent surface biocompatibility[29]. For instance, Nakamura et al[30]. developed a planar solution-gated FET (SGFET) utilizing diamond, where DNA-immobilized channels are directly interfaced with electrolytes. The attachment of DNA via amine sites significantly enhances sensor sensitivity, enabling the discrimination of 3-mer mismatches within 21-mer DNA oligonucleotides at concentrations as low as 10 pM.

In contrast to traditional silicon-based ISFETs, the BDD-SGFET does not necessitate a separate insulating layer, allowing its surface to be directly exposed to the electrolyte, which enhances the conduction of electrochemical signals. Given the significant influence of surface termination species on the electrochemical performance of diamond, particularly with respect to its active surface area, current research on boron-doped diamond solution-gated field-effect transistors (BDD-SGFETs) has primarily focused on hydrogen and oxygen as the two main types of termination species[31]. The hydrogen-terminated diamond surface features a two-dimensional hole gas (2DHG) channel that does not require external doping, endowing it with p-type semiconductor characteristics. The introduction of hydrogen termination to induce p-type behavior in the surface channel was initially demonstrated by Kawarada et al.[32]. However, the electrochemical activity of hydrogen-terminated diamond is highly contingent on the specific surface state, with alterations in the hydrogen-terminated surface affecting the current-voltage (I-V) characteristics of BDD-SGFETs, leading to susceptibility to oxidation[33]. In contrast, the oxygen-terminated diamond surface is noted for its high corrosion resistance, making it suitable for applications in electrochemical analysis and wastewater treatment[34,35]. Despite the advantages, developing oxygen-terminated diamond FET structures with low threshold voltage and high transconductance has proven challenging due to the absence of shallow dopants. To conquer these dilemmas, researchers have made ongoing advancements[36,37]. In this regard, Edgington et al.[38] first suggested a solution utilizing a boron-oxidized δ-doped channel on (111) diamond, investigating the SGFET's sensitivity to solution pH. The performance of this device rivals that of hydrogen-terminated diamond surfaces and exhibits improved stability. Research by Švorc et al.[39] has demonstrated that boron-doped diamond electrodes maintain long-term electrochemical stability in complex biological fluids. Nevertheless, significant efforts remain necessary to develop high-performance BDD-SGFETs.

Current investigations into diamond-based FETs have predominantly centered on planar architectures, where

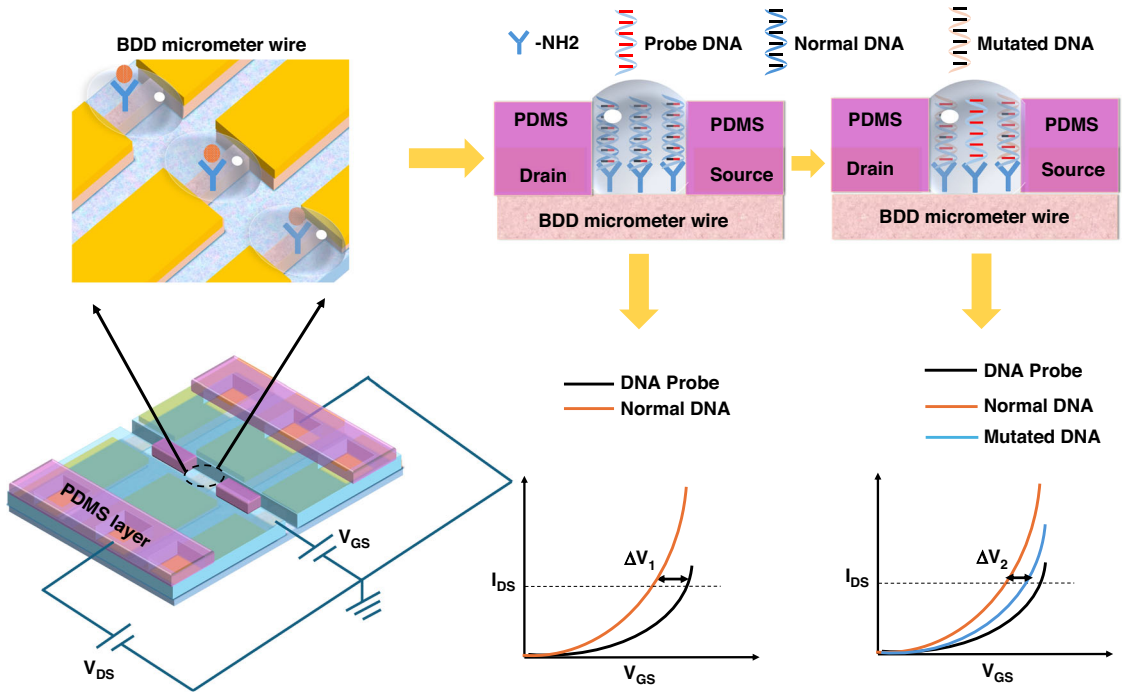

Fig. 1 Schematic representation of both the structure and the principle of the BDD-SGFET biosensor for mutant gene detection

the constrained specific surface area limits sensitivity. Hideshima et al.[40] improved sensor performance by integrating nanoscale dimensions with FET architectures, achieving the detection of influenza A virus hemagglutinin molecules. Thus, the sensing capabilities of these devices can be substantially enhanced by engineering micro/nanostructures within the channel region of solution-gated diamond FETs. The advancement of diamond micro/nanostructures with high specific surface areas and controllable morphologies has thus emerged as a crucial technological strategy for realizing high-performance boron-doped diamond solution-gated FET (BDD-SGFET) channels.

A high-performance BDD-SGFET biosensor with microwires is presented for the label-free detection of base mismatches associated with gene mutations (Fig. 1). The influence of diamond microwire size on the electrical properties of the BDD-SGFET was evaluated through Silvaco TCAD simulations. Subsequently, three-dimensional (3D) microwire structures were fabricated on the boron-doped diamond film using microfabrication techniques, including photolithography and plasma etching. This innovative structure enhances the specific surface area of the sensing region and increases gate capacitance, thereby achieving improved sensor performance. By employing suitable sensor surface functionalization and the immobilization of DNA probes, the fabricated BDD-SGFET is capable of distinguishing target DNAs with varying numbers of base pair mismatches. Furthermore, a series of experiments involving concentration gradients across different orders of magnitude and subsequent performance characterization reveal that the BDD-SGFET demonstrates remarkable sequence selectivity, robust anti-interference capabilities in complex environments, and high reproducibility. This work specifically assesses the ability of the fabricated BDD-SGFET to identify and detect DNA sequences featuring various types of base mutations, including single-base and multi-base mutations. This development provides a promising novel tool for the analysis of genetic variation and the early diagnosis of disease.

Result and discussion

Structural simulation and optimization of BDD-SGFET

Before the fabrication and testing of BDD-SGFET, rational simulations were employed to determine appropriate dimensional parameters and to verify stable, reasonable electrical properties. This approach not only enhances the reliability of experimental results but also effectively reduces fabrication and time costs. In this study, Silvaco TCAD software was utilized to simulate BDD-SGFET, with the aim of guiding subsequent device fabrication and performance validation. Specifically, the DevEdit module of TCAD was employed to construct a three-dimensional device model, while the Atlas module was implemented to simulate the electrochemical properties of the device. For detailed information on the simulation model and Simulation

principle, the readers are referred to the Supplementary Materials (Fig. S1).

Based on the simulation model of BDD-SGFET, the electrical properties of the device were analyzed by varying the dimensions of the diamond microfilaments within the BDD-SGFET. As illustrated in Fig. 2, simulations a,b and c depict the output characteristic curves of micro wire BDD with a fixed length of 100 microns, while widths were varied at 5, 10, and 20 microns, respectively. The results demonstrate a linear increase in I_{DS} as the drain-source voltage scanning range was from 0 to −1V. Additionally, a varying increase in drain-source current was observed as the gate voltage rose from 0 to −0.4 V, consistent with FET behavior, thereby affirming the validity of the simulation. Notably, as the width of the microfilament increased, the drain-source current also exhibited an increase. The transfer characteristics simulated in Fig. 2d further corroborated these findings, indicating that at a drain-source voltage of −0.5 V and a gate voltage scan from 0.5 V to −0.5 V, the drain-source current gradually increases, with the gradual rising of slope until attaining its maximum around a gate voltage of −0.4 V. Taking this slope for transconductance, the calculation results demonstrate that the width increases with the transconductance.

Similarly, in Fig. 2, simulations e,f and g illustrate the output characteristic curves of micro wire BDD at a fixed width of 30 microns, with lengths varied at 600, 300, and 150 microns. The results trend indicated a relatively linear increase in I_{DS} over the drain-source voltage scanning range of 0 to −1V. However, an increase in length correlated with a decrease in drain-source current. The transfer characteristic curve depicted in Fig. 2h confirmed that, at a drain-source voltage of −0.5 V and a gate voltage scanning from 0.5 V to −0.5 V, the drain-source current increased, with the slope gradually rising until reaching a maximum value at approximately −0.4 V. The transconductance calculated from this slope demonstrated a decrease in transconductance with increasing length.

The simulation results substantiate that both the length and width of the diamond microwire have a profound influence on the device's electrical performance. Under ideal testing conditions, increasing microwire width or decreasing length enhances the control over I_{DS}. Nonetheless, actual fabrication and testing of BDD-SGFET are subject to various limitations. Therefore, considering the limitations and potential errors inherent in manufacturing processes, the diamond microwires produced in subsequent steps will be approximately 100 μm in length and 10 μm in width.

Manufacture of BDD-SGFET

Based on the aforementioned simulation results of the BDD-SGFET, the device was fabricated in accordance with the optimized simulation model structure. The overall preparation process is illustrated schematically in Fig. 3a. To this end, a 200 nm-thick boron-doped diamond (BDD) film was first grown on a single-crystal diamond substrate using MPCVD. Following this, a mask was fabricated, and photoresist was spin-coated onto the surface, which was subsequently baked at 100 °C for 2 min. The photoresist was patterned via mask lithography, with an exposure time of 2.3 s and a development phase lasting 45 s. After cleaning, the BDD film underwent plasma etching to form microwires, followed by the removal of the photoresist. Subsequently, a 20/200 nm Cr/Au film was deposited to establish the source and drain regions. A silicon dioxide (SiO_2) layer was then deposited in SiH_4 gas utilizing plasma-enhanced chemical vapor deposition (PECVD) to serve as the insulating layer, with the channel and electrode areas exposed through photolithography. Finally, the device was encapsulated with epoxy resin. The three-dimensional (3D) structure of the final device is schematically represented in Fig. 3b, featuring a three-layer configuration.

Figure 3c presents the fabricated device, which comprises three BDD-SGFETs isolated by epoxy resin and SiO_2. The regions circled in red within subfigures (I), (II), and (III) correspond to the three microwires and the detection area, respectively. The production method and dimensions of the three microwire structures are consistent. Figure 3d displays the scanning electron microscope (SEM) image of the microwire region, with microwires measuring 7.68 μm in length and 100.8 μm in width, yielding an aspect ratio (W/L) of approximately 0.08. This particular ratio contributes significantly to the excellent performance of the device.

Electrochemical performance of BDD-SGFET

To assess the electrochemical performance, the fabricated BDD-SGFETs were characterized experimentally. The specific operating principle is detailed in the Supplementary Materials (Fig. S2). Hall effect measurements revealed a hole carrier concentration of 7.7×10^{19} cm^{-3} in the BDD film. This carrier density, significantly surpassing 10^{13} cm^{-3}, effectively reduces contact resistance, thus enhancing the current drive capability of the subsequent devices[41]. Given that ohmic contact resistivity (ρ_c) is a critical factor for device performance, the transmission line method (TLM) was employed for characterization (Fig. 4a). The measured resistance (R_T) correlates with the ratio of the outer ring diameters (R) to inner ring diameters (r). A ρ_c magnitude of 4.47×10^{-4} $\Omega \cdot cm^2$ was extracted, which is lower than previously reported values for BDD-SGFETs[42,43], suggesting that the diamond microwire architecture effectively optimizes the contact interface.

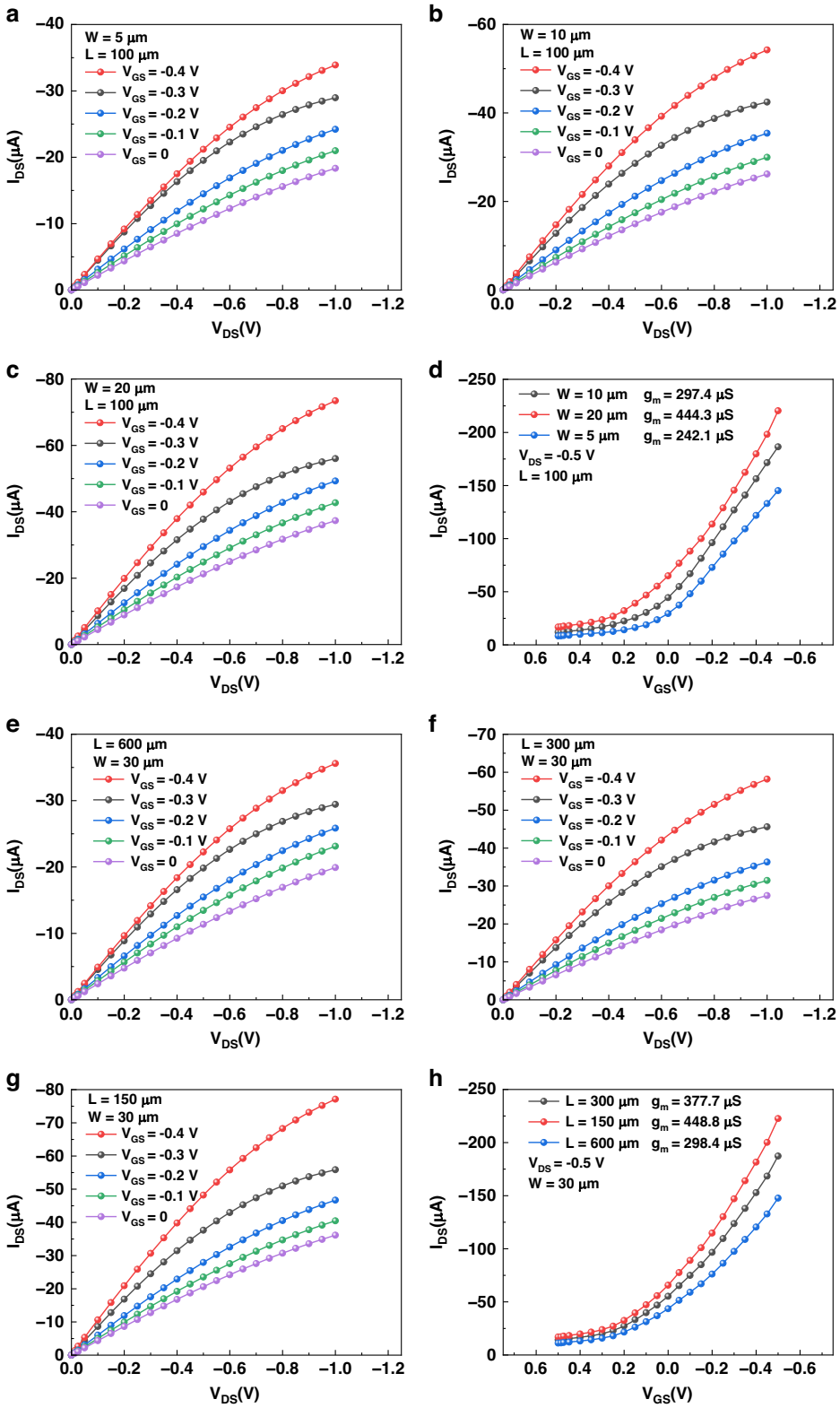

Fig. 2 Simulation of electrochemical performance for various gate channel dimensions. a–**c** Present output characteristic curves with varying widths of 5, 10, and 20 micrometers for a length of 100 micrometers, respectively. **d** Transfer characteristic curves for various widths. **e**–**g** Present output characteristic curves with varying widths of 600, 300, and 150 microns when the width is 30 microns, respectively. **h** Transfer characteristic curves with various lengths

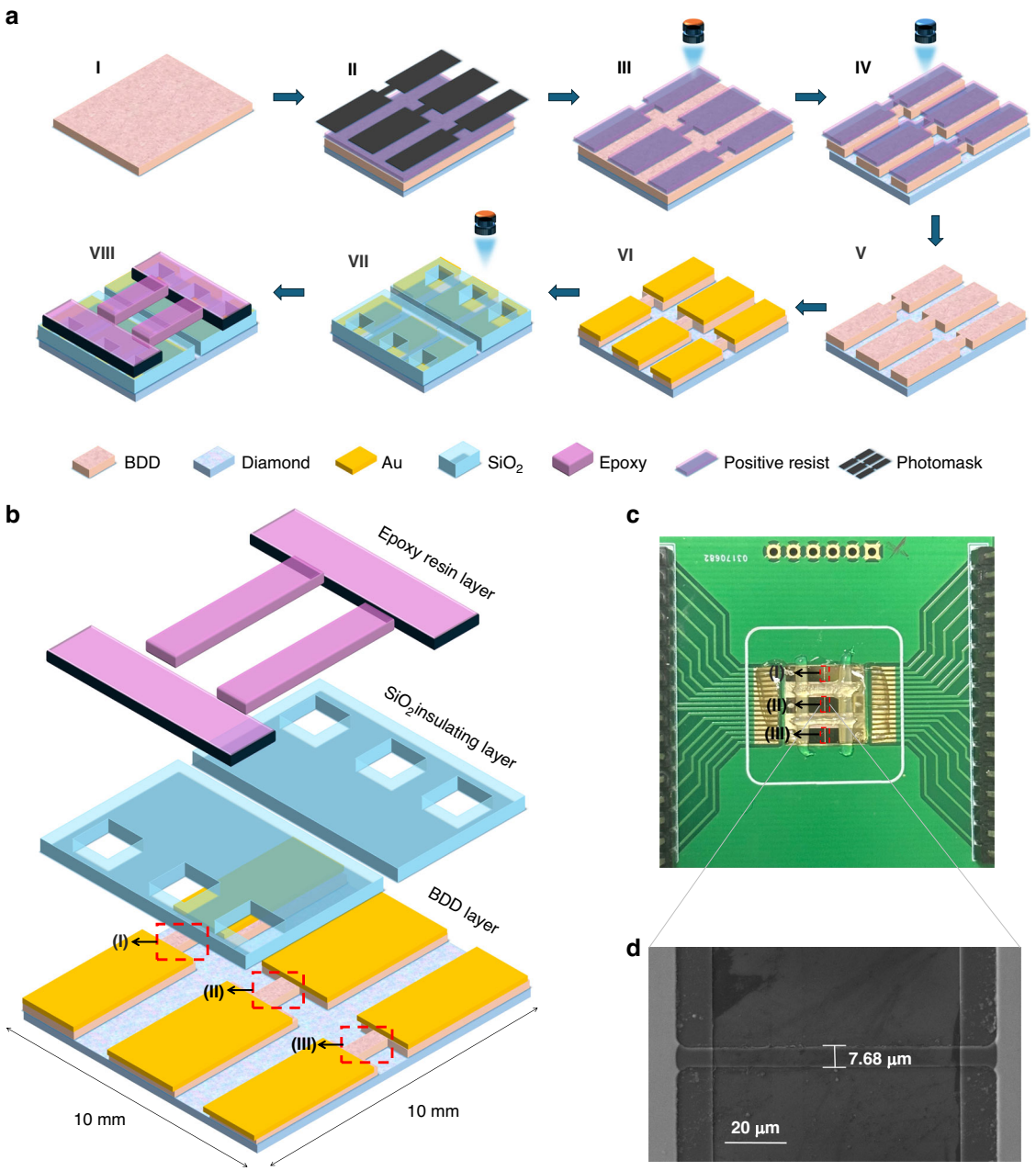

Fig. 3 Schematic representation of the BDD-SGFET structure. a Fabrication protocol for BDD-SGFET. (I) MPCVD growth of boron-doped diamond, (II) Manufacturing mask plates and spin-coating, (III) Etching photoresist through mask lithography (IV) Plasma etching of boron-doped diamond, (V) Remove glue, (VI) Gold-plated electrode, (VII) Deposition of SiO_2 insulation layer, (VIII) Epoxy resin encapsulation. **b** Dimensions of the BDD-SGFET structure. **c** Image of BDD-SGFET (*note*: Subfigures (I), (II), and (III) correspond to three microwires and the detection area, respectively). **d** SEM image of oxygen-terminated BDD-SGFET morphology. Scale bar: 20 μm

The output characteristics of the BDD-SGFETs were further analyzed. As illustrated in Fig. 4b, when V_{DS} varies from 0 V to −1 V, I_{DS} gradually increases, reaching a maximum at $V_{DS} = -0.6$ V. This indicates that when the BDD-SGFET's operating potential exceeds −0.6 V, I_{DS} is predominantly influenced by external analytes. Concurrently, an increase in V_{GS} (here used to simulate changes in target molecules) results in a synchronous increase in I_{DS}. At $V_{GS} = -0.4$ V, the device demonstrates a maximum output current ($I_{DS,max}$) of −3.3 mA/mm. Figure 4c displays the transfer characteristics and transconductance distribution curve of the device, highlighting a maximum transconductance ($g_{m,max}$) of approximately 289 μS/mm. Figure 4d demonstrates that the threshold

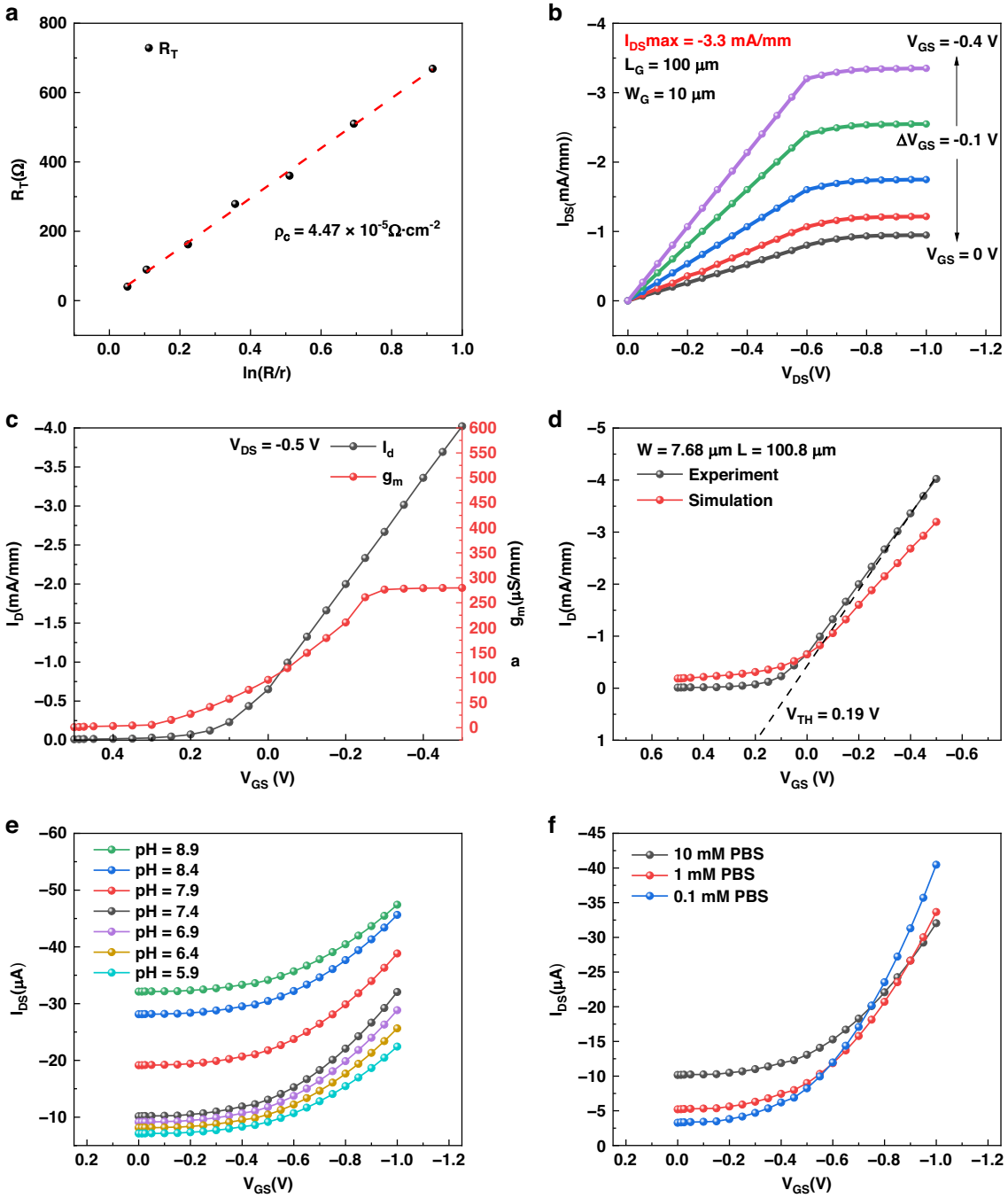

Fig. 4 Electrical characterization of the BDD-SGFET device. a *ln (R/r) - R_T* line of the BDD-SGFET. **b** I_{DS}–V_{DS} curves with V_{GS} varying from 0 to −0.4 V. **c** I_d–V_{GS} curve and g_m-V_{GS} curve of the BDD-SGFET device. **d** Comparison graph of the transfer characteristic curves and the simulation results. **e** I_{DS}–V_{GS} curves of the BDD-SGFET measured under various pH conditions in 10 mM PBS. **f** I_{DS}–V_{GS} curves of the BDD-SGFET measured with various dilutions of PBS at pH 7.4

voltage (V_{TH}) extracted from the V_{GS}-I_D relationship of the fabricated BDD-SGFET is 0.19 V, indicating a normally-on mode. Notably, the trend and values of the V_{GS}-I_{DS} relationship obtained from simulations align closely with those of the fabricated BDD-SGFET, further validating the simulations and underscoring their guiding role in the fabrication process. For the same gate length, the $I_{DS,max}$ achieved by the BDD-SGFET in this work is over 40 times higher than that of existing MESFETs[44] and more than 60 times greater

than that of MOSFETs[45], achieving a high current level (Table S3).

Recognizing that the operation of a BDD-SGFET necessitates the immersion of the gate electrode in an electrolyte, the physicochemical properties of this liquid environment significantly impact the device's detection capabilities. Therefore, we systematically evaluated the performance of the fabricated BDD-SGFET by modulating the ionic concentration and pH of the gate solution. These investigations elucidate the fundamental sensing characteristics of the device, thereby establishing a robust foundation for its subsequent application in mutant gene detection.

Figure 4e illustrates the variations in the transfer characteristic curves of the oxygen-terminated BDD-SGFET within a 10 mM PBS buffer across various pH values, with the V_{GS} scan range set from 0 to −1 V. The results reveal an overall increase in I_{DS} with rising pH, peaking in transconductance at pH = 7.4. This special behavior can be attributed to the electrochemical properties inherent to the oxygen-terminated surface. Following oxidation treatments, such as oxygen plasma treatment, the surface of the BDD-SGFET acquires oxygen-containing functional groups, including C = O, C-OH, and C-O-C. These functional groups exhibit amphoteric properties, enabling them to undergo reversible protonation/deprotonation reactions with H^+ ions present in solution. In more acidic environments, lower pH values elevate the H^+ concentration, resulting in the protonation of these functional groups and the formation of more positively charged groups. This effect is analogous to the application of an additional positive gate voltage to the BDD-SGFET surface, which diminishes carrier concentration in the p-channel (i.e., hole conduction) and leads to decreased device conductivity. Conversely, under more alkaline conditions, elevated pH values increase the OH^- concentration in the solution, causing deprotonation of the oxygen-containing functional groups and resulting in a greater number of negatively charged groups. This mirrors the application of an additional negative gate voltage, which enhances hole attraction in the p-type channel, facilitating the device's activation. The transconductance is also affected by carrier mobility, with higher mobility correlating to greater transconductance. Close to the neutrality conditions, the surface exists in a partially protonated state characterized by minimal net charge (potentially near the isoelectric point) yielding the weakest local electric field at the interface. Therefore, the scattering of ions on channel carriers is minimized, resulting in the highest carrier mobility and thus maximum transconductance. Under these circumstances, the BDD-SGFET demonstrates peak electrochemical performance at a pH of 7.4. Thus, employing pH = 7.4 as the optimal testing condition guarantees device characterization at an ideal operating point, mitigating the influence of environmental pH fluctuations on performance.

Figure 4f presents the variation of transfer characteristic curves of the oxygen-terminated BDD-SGFET at pH=7.4 in the presence of various PBS buffer concentrations. The obtained results are indicative of the fact that as the PBS buffer concentration increases, the overall I_{DS} shifts upward along the axis, while the curve trend becomes flatter. This effect arises because an increase in PBS buffer concentration diminishes the solution's Debye length[40]. The presence of high-concentration ions within the solution facilitates the formation of an efficient "electrostatic shielding layer", which confines the electric field generated by the applied gate voltage to a region immediately adjacent to the BDD-SGFET surface. As a result, the electric field becomes less effective in penetrating and modulating the entire channel, significantly limiting the gate voltage's capacity to control current. This is observed as a reduction in transconductance and a flatter curve.

In summary, the exceptional transport characteristics, characterized by high transconductance (g_m) and low threshold voltage (V_{TH}), are primarily a result of the superior surface quality of the microfilament structures achieved through the photolithography and etching techniques developed in the current study. Therefore, the fabricated BDD-SGFET exhibits remarkable electrical performance, indicating strong potential for the detection of mutant DNA. Additionally, the optimization of electrolyte conditions (10 mM concentration at pH = 7.4) provides a conducive environment that further enhances the reliability and sensitivity of subsequent DNA sensing assays.

Mutation DNA molecular detection based on BDD-SGFET

The detection of gene mutations is essential for elucidating disease mechanisms at the molecular level, facilitating early diagnosis and enabling targeted therapies. This process forms a fundamental aspect of contemporary precision medicine. Using non-small cell lung cancer as a case study, the BDD-SGFET device developed in this research was employed to accurately identify mutations characterized by varying numbers of base pairs within specific DNA fragments.

The advantages of BDD-SGFET for mutant DNA detection were validated through the modification process, and the response results obtained when detecting mutant DNAs with differing base pair counts (Fig. 5). As depicted in Fig. 5a, a series of experimental procedures were implemented to achieve effective mutant DNA detection. Specifically, the fabricated BDD-SGFET underwent treatment with oxygen plasma to introduce hydroxyl groups on the channel surface. This step was followed by treatment with 3-aminopropyltriethoxysilane (APTES) to functionalize the surface with amino groups,

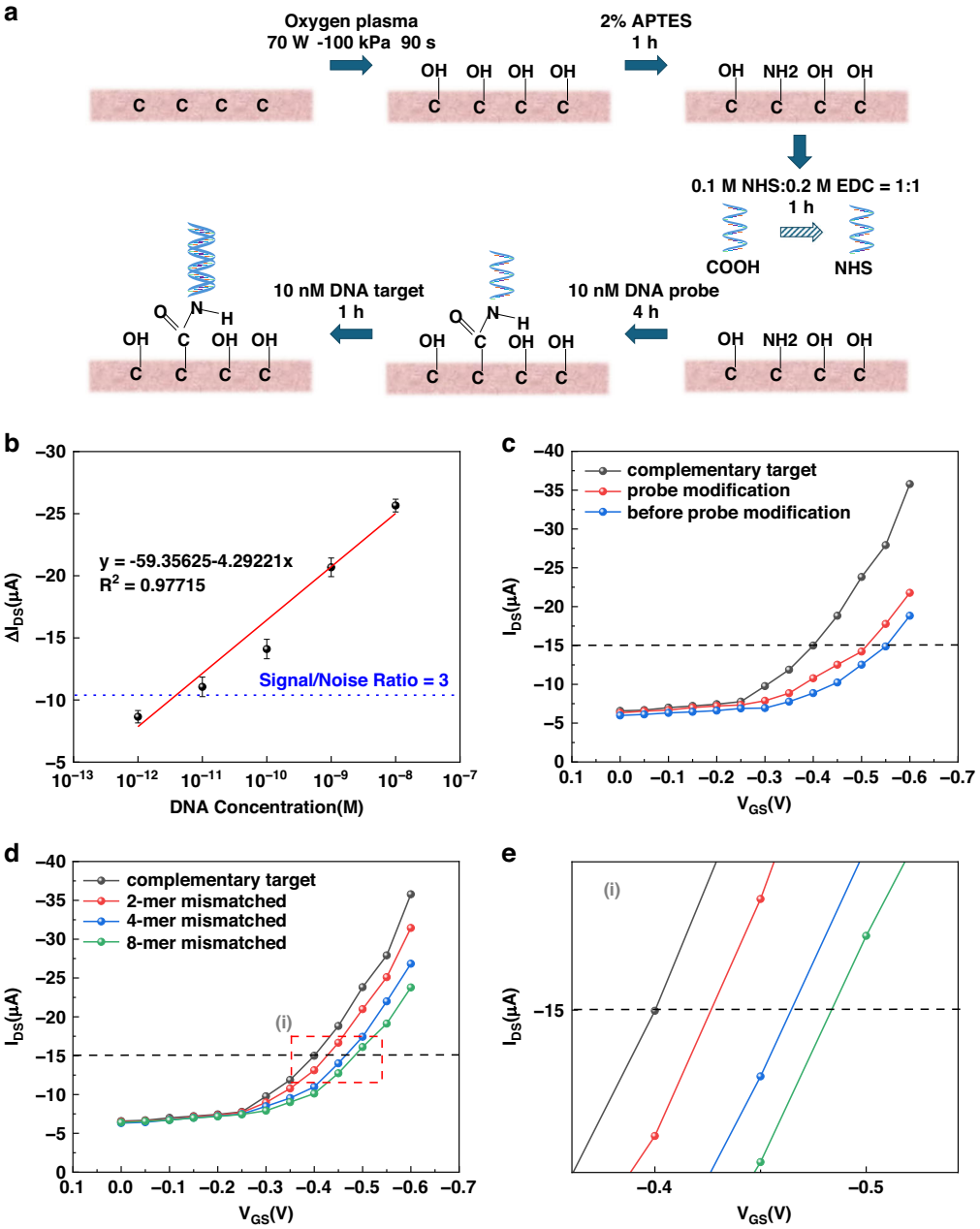

Fig. 5 BDD-SGFET-based Mutation DNA molecular detection. a Schematic representation of BDD-SGFET modified DNA process. **b** ΔI_{DS} of the BDD-SGFET at a series of DNA concentrations. **c** Transfer curves of the normal target and DNA probe hybridization via BDD-SGFET. **d** Transfer curves of DNA probe hybridization using various numbers of mutant base pairs using BDD-SGFET (*note*: The concentration of probes and different mismatched targets is 10 nM). **e** Gate offset of DNA probe hybridization using different numbers of mutant base pairs

which were subsequently activated via a mixed solution of N-hydroxysuccinimide (NHS) and 1-ethyl-3-(3-dimethylaminopropyl) carbodiimide (EDC). The process culminated in the immobilization of DNA probes on the channel surface, completing the preprocessing of the BDD-SGFET. For the detection stage, the target DNA solution was applied directly to the BDD-SGFET for hybridization. After hybridization, the device was thoroughly washed, followed by the application of a buffer solution for direct detection. Finally, the BDD-SGFET was placed on a heating platform to facilitate the dissociation of the hybridized DNA.

Sensitivity is a critical parameter for assessing the performance of biosensors, as it directly influences the minimum detectable concentration of the target analyte. To evaluate the response capability of the fabricated

BDD-SGFET to DNA hybridization events and to ascertain the minimum detectable DNA concentration, its detection sensitivity was systematically quantified (Fig. 5b). The sensitivity response of the sensor was characterized through DNA hybridization experiments designed with concentration gradients. Specifically, single-stranded DNA probes with known sequences were immobilized on the sensor surface. The sensor was then hybridized with target DNA sequences of known but varying concentrations, ranging from 1 pM to 10 nM. After each DNA hybridization step at various concentrations, the change in drain-source current (ΔI_{DS}) in the presence of a fixed bias voltage was accurately measured, and this change was subsequently analyzed to evaluate the sensitivity performance of the fabricated BDD-SGFET. The ΔI_{DS} value was defined as the difference between the current post-hybridization and the baseline current measured after probe immobilization, reflecting the charge change induced by DNA hybridization on the sensor surface. A blank control group was also included to establish the background noise level of the system and to ensure the validity of the data. The experimental results demonstrated that ΔI_{DS} increased systematically with the elevation of the concentration of complementary DNA targets (Fig. 5b). Within the concentration range of 1 pM to 10 nM, ΔI_{DS} exhibited a robust linear relationship with the logarithm of the target DNA concentration. This linear response confirms the quantitative capability of BDD-SGFET for analyzing DNA concentration. The experimental limit of detection was determined based on the signal-to-noise ratio (SNR) criterion, which dictates that the effective signal must be at least three times the background noise. The noise level observed in the triple blank control group was 11.2 μA. Although the signal at a DNA concentration of 10 pM (12.3 μA) significantly surpassed this noise threshold, the signal at 1 pM (8.4 μA) remained below this threshold and was thus deemed invalid. Consequently, the actual limit of detection for the sensor was determined to be 10 pM. This exceptional sensitivity can be attributed to the synergistic advantages of the BDD material along with the FET device architecture.

The transfer characteristics of BDD-SGFET, following modification and DNA detection, are illustrated in Fig. 5c. In this instance, both the DNA probe and DNA target concentrations were set to 10 nM. The results indicate that the I_{DS} increases to a notable extent after both DNA probe immobilization and target DNA hybridization. Specifically, when the I_{DS} measures −15 μA, the V_{GS} shifts leftward by 40 mV after DNA probe immobilization and by 150 mV following DNA hybridization. This behavior is primarily due to the hybridization of the probe oligonucleotide with the complementary oligonucleotide, resulting in an increased hole density attributed to the enhanced negative charge on the p-type channel surface[46]. Therefore, the gate potential experiences a positive shift, causing an increase in drain current (The detailed principle of BDD-SGFET for detecting gene mutations can be found in Supplementary Material Fig. S2).

Subsequently, the detection capability of BDD-SGFET for mutant DNA was assessed by investigating DNAs with varying numbers of mutated base pairs (Fig. 5d–e). As depicted in Fig. 5d, an increase in the number of mutated base pairs in DNA correlates with an increase in I_{DS} for BDD-SGFET, although the variation in I_{DS} diminishes. Specifically, the I_{DS} approaches the value observed after DNA probe immobilization when the number of mutated base pairs reaches 8. Based on the previously discussed principles of DNA probe immobilization, the I_{DS} is influenced by the EDL capacitor. The hybridization of normal DNA strands forms a regular, rigid, and compact double-stranded DNA layer, which maximizes its impact on I_{DS} under other constant conditions, yielding the minimum I_{DS} for normal DNA detection. In contrast, mutant DNA introduces base mismatches, resulting in the formation of defective, loose, and more flexible DNA strands. This leads to a disordered and dispersed distribution of negative charges, whereas unhybridized DNA fragments extend into the solution like “floccules”, increasing the average effective distance between negative charges and the channel surface[47]. This loose structure ultimately elevates the equivalent distance of the charge layer, reduces capacitance, and diminishes the ability to control the total parallel capacitance, effectively decreasing gate voltage modulation efficiency. Consequently, for the same applied gate voltage, the charge variation in the channel decreases, resulting in a reduced variation amplitude of I_{DS}. As the number of mutated base pairs increases, the hybridized DNA strands become less stable, which diminishes the gate voltage control capability and leads to a reduced variation in I_{DS}. Consequently, the I_{DS} is lower when the number of mutated base pairs is higher compared to scenarios with fewer mutations. This behavior facilitates accurate detection of varying numbers of mutated base pairs.

To further assess the mutant DNA detection performance of the BDD-SGFET, the V_{GS} shifts following hybridization with DNAs containing different numbers of mutated base pairs were quantified (Fig. 5e). The data illustrate that at an I_{DS} of -15 μA, DNAs with differing numbers of mutated base pairs exhibit distinct V_{GS} shifts. Specifically, the gate voltage shifts associated with complete complementary hybridization for the 2-mer, 4-mer, and 8-mer groups in order are 26 mV, 64 mV, and 83 mV. It is worth noting that the gate voltage shift here is relative to the complete target DNA hybridization signal, and this trend is qualitatively consistent with the theoretical trend calculated by Equations 4–6 in the

Supplementary Materials (where the theoretically calculated gate voltage shifts associated with the fully complementary hybridization of dimer, tetramer and octamer groups are 33.9 mV, 43.9 mV and 54.5 mV). Non-uniform probe distribution on the surface of actual devices, non-specific adsorption, and fluctuations in environmental conditions can lead to discrepancies between theoretical calculations and experimental measurements. The theoretical model assumes that DNA probes form an ideal monolayer—uniform, closely packed, and perfectly ordered—on the gate surface, under uniformly ideal experimental conditions. In practical scenarios, however, the immobilization density of DNA probes is inherently non-uniform, and a degree of non-specific binding is inevitably introduced during the DNA hybridization process. Free target DNA molecules may undergo physical adsorption onto the boron-doped diamond (BDD) surface, and the negative charges they carry can perturb the charge density distribution within the Debye length. Moreover, experimental conditions cannot be perfectly controlled across different runs; variations in ambient environment, experimental parameters, and operational procedures are unavoidable. These factors collectively contribute to the observed deviations between theoretical predictions and experimental measurements. Nevertheless, despite these discrepancies, the overall trends in gate voltage shift remain consistent. The magnitude of the shift varies systematically with the number of base pair mismatches. This trend indicates an increase in the magnitude of the gate voltage shift with a higher number of base-pair mutations. A greater number of base-pair mutations contributes to the instability of the hybrid, making it more susceptible to deformation or the formation of defective structures. As a result, hybridization efficiency diminishes, leading to a lower stable binding of molecules and a reduction in the exposed negatively charged backbones. Thus, the post-hybridization current for hybrids with a larger number of mutated base pairs approaches the baseline current (post-probe immobilization) more closely than that of hybrids with fewer mutations[48].

In summary, the pronounced gate voltage offset effectively captures charge variations during DNA hybridization. This device reliably differentiates between unmutated DNA and DNA with various mutations in base pairs, demonstrating the exceptional electrical response characteristics and sequence selectivity of the microwire BDD-SGFET. It holds promise for biosensing applications, including biomolecular recognition and gene mutation detection.

Reliability characterization of BDD-SGFET

To verify the repeatability of the device, we designed a dissociation experiment after hybridization with different base pair mutations. In the current investigation, the repeatability of the fabricated BDD-SGFET was assessed by repeating the processes of DNA hybridization and dissociation with varying numbers of mutant base pairs (Fig. 6a–b). As illustrated in Fig. 6a, the change in I_{DS} remained consistently stable after hybridization and dissociation with DNAs containing different numbers of mutant base pairs, demonstrating that the fabricated BDD-SGFET exhibits commendable repeatability. It is noteworthy that a discernible difference was observed between the I_{DS} generated by the sensor modified only with DNA probes and that generated by the sensor undergoing DNA hybridization and dissociation processes. This difference primarily arises from incomplete dissociation, which does not affect the experimental results under controlled operational conditions. To further validate repeatability, multiple tests were conducted, and the changes in I_{DS} were normalized (Fig. 6b), where I_0 denotes the initial current after DNA probe modification, and ΔI signifies the current change after achieving maximum current stability. As depicted in the figure, the multiple repeated experiments exhibited small trend error bars and a relatively smooth profile. After hybridization and dissociation with DNAs containing differing numbers of mutant base pairs, the changes in electrical signals remained approximately unchanged, further substantiating the good repeatability of the fabricated BDD-SGFET.

To evaluate the stability of the BDD-SGFET, DNA molecule detection was conducted at regular intervals (every 5 days), with the device stored in a moisture-proof cabinet at 20 °C and a relative humidity (RH) of 10%, and then, the transfer characteristics were analyzed (Fig. 6c). As indicated in the figure, with an increase in the sensor's storage time, I_{DS} gradually lessened. This phenomenon is primarily due to the susceptibility of DNA probes to environmental factors. Over time, the DNA probes modified on the sensor become increasingly inactive, leading to heightened resistivity and a resultant reduction in current. To further affirm the sensor's stability, additional repeated experiments were conducted (Fig. 6d). The obtained results demonstrated a decline in I_{DS}. Notably, compared to earlier measurements, the I_{DS} decreased by approximately 17.54% and 25.31%, respectively. This decline is mainly attributed to the gradual increase in channel resistivity over time. In summary, the fabricated BDD-SGFET exhibits both good repeatability and a degree of long-term stability.

To verify the anti-interference capability of the device, a 1 mg/mL lysozyme solution in 10 mM PBS buffer (pH = 7.4) was employed as the blank control in subsequent experiments. The transfer characteristics of DNAs with varying numbers of base-pair mutations were methodically examined in the presence of the lysozyme solution (Fig. 6e), where I_0 signifies the maximum current after

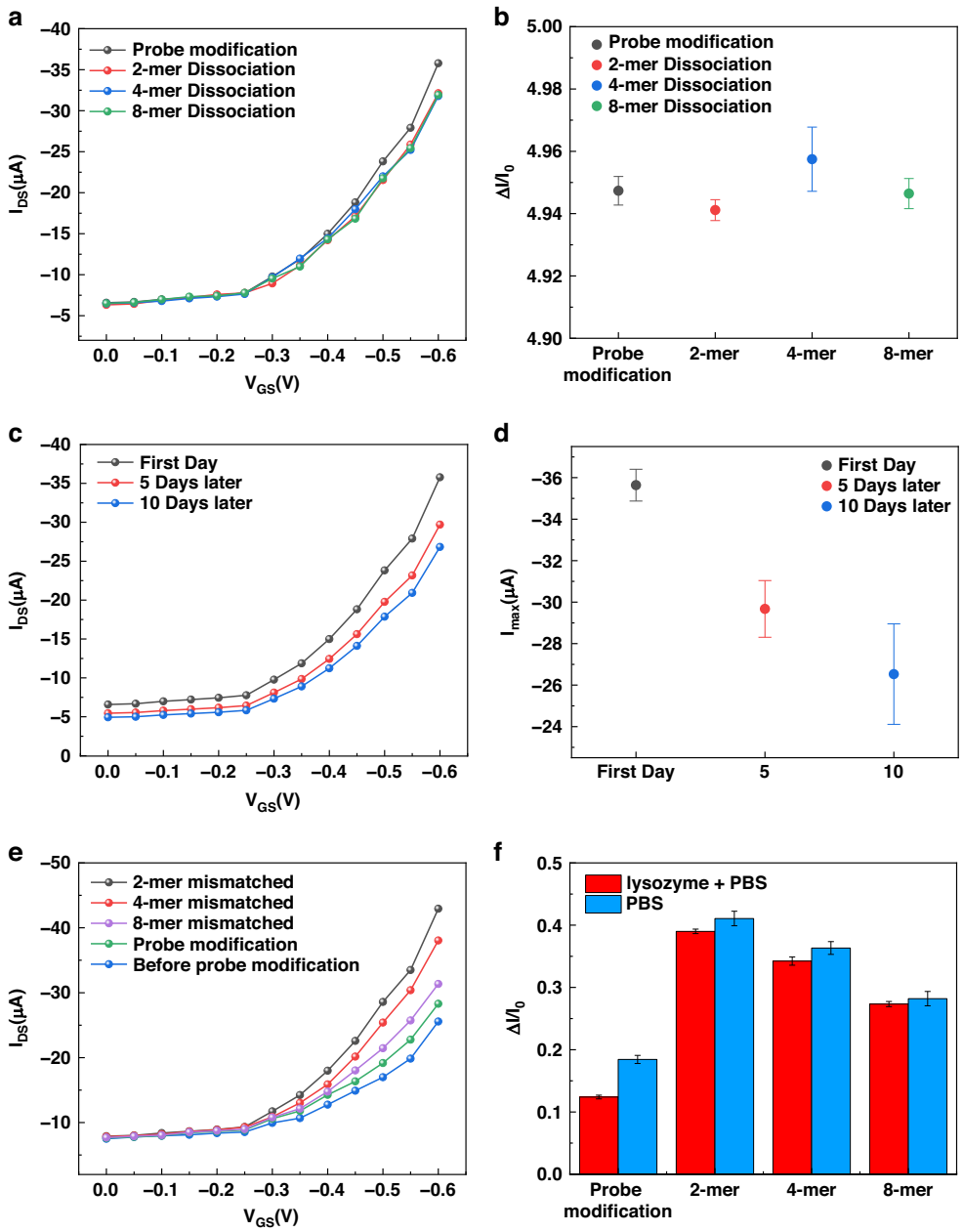

Fig. 6 Reliability characterization of the BDD-SGFET structure. a Transfer characteristic curves of DNA with various numbers of base pairs mutated after dissociation. **b** Comparison of electrochemical signals after dissociation of mutated DNA with various numbers of base pairs and only modified DNA probes. **c** Test the transfer characteristic curves of the devices on the first, fifth, and tenth days respectively. **d** The maximum current in the transfer characteristic curve of the device was detected on the first, fifth, and tenth day, respectively. **e** Transfer curves of target probe hybridization with various numbers of base pair mutations under the background of adding 1 mg/mL lysozyme. **f** Comparison of the current signal response before and after adding lysozyme

probe modification, and ΔI represents the stable current change. As illustrated in the figure, the overall trend of the I_{DS} induced by DNAs with various base-pair mutations remained largely unaffected following the addition of lysozyme. This observation can be attributed to the specific binding characteristics of the DNA probes modified during the fabrication of BDD-SGFET, which exhibit hard binding to lysozyme, thereby avoiding interference with the sensor's detection results. This indicates that the fabricated BDD-SGFET demonstrates exceptional anti-interference capability. The relationship between the number of base-pair mutations and the current change

rate following probe hybridization was further corroborated through multiple repeated experiments (Fig. 6f). As depicted, the overall level of I_{DS} decreased after the addition of lysozyme, while the intensity of signal change diminished. This phenomenon is primarily due to lysozyme (with an isoelectric point pI~11) possessing a substantial number of positive charges under typical physiological buffer conditions (PBS, pH = 7.4). The adsorption of positively charged lysozyme repels holes, resulting in a decrease in current. However, the extent of this current reduction is limited and insufficient to lead to significant interference with the experimental results. In conclusion, the BDD-SGFET exhibits outstanding detection performance for quantifying various base-pair mutations in ctDNA, highlighting its considerable potential in the field of genetic mutation detection.

Conclusion

This paper introduces a high-performance microwire BDD-SGFET biosensor designed for the label-free detection of base mismatches resulting from gene mutations. Through Silvaco TCAD simulations of the BDD-SGFET, the effects of the length and width of diamond microwires on the electrical properties of the device were examined. Microscale manufacturing was achieved on a BDD layer with a boron doping concentration of 7.7×10^{19} cm^{-3} and a thickness of 200 nm, utilizing photolithography and plasma etching techniques. The fabricated device features a gate length of 100.8 μm and a gate width of 7.68 μm, with a maximum output current of 3.3 mA/mm. The transconductance of the BDD-SGFET reaches 289 μS/mm, remarkably surpassing values reported in previous investigations. This sensor demonstrates high sensitivity (detection limit of 10 pM). Utilizing this characteristic, the detection of EGFR, a biomarker for non-small-cell lung cancer, serves as an example, successfully identifying DNA molecules with two base-pair mismatches within a sequence of 21 base pairs. Furthermore, the device exhibits good repeatability and stability over a relatively short time frame, demonstrating its feasibility for biosensing applications. This device enables the detection of mutant DNA, presenting a promising novel tool for the analysis of genetic variation and early disease diagnosis.

Materials and methods

Growth of boron-doped diamond thin film

The BDD epitaxial layer was deposited on a 10 × 10 mm single-crystal diamond substrate utilizing MPCVD. The specific growth conditions included a methane/hydrogen ratio of 6%, a growth temperature of 1050–1060 °C, microwave power set to 6500 W, and a pressure of 90 torr. A pre-mixed gas of diborane/methane (B_2H_6/CH_4, at 5000 ppm) served as the p-type dopant source, resulting in a uniform BDD layer that attained a thickness of approximately 200 nm. The electrical conductivity of the diamond after boron film deposition was assessed using a four-terminal measurement system (model DCA-100, Jiaxing Worldia Diamond Tools Co., Ltd.), yielding a conductivity value of 6.16 $cm^2 \cdot V^{-1} \cdot s^{-1}$. The surface roughness measurements, conducted with a Surftest SJ-4101 profilometer, indicated an average roughness (R_a) of 5 nm and a maximum roughness (R_{max}) of 6 nm. Hall effect measurements further established a p-type carrier concentration of around 7.7×10^{19} cm^{-3} and a sheet resistance of 4.52×10^3 Ω/sq.

BDD-SGFET fabrication

The manufacturing process for BDD-SGFET primarily involves several steps: BDD growth, BDD patterning, BDD insulating layer deposition, exposure of the sensing and electrode regions, and final sensor encapsulation. Initially, after the MPCVD growth of the BDD, the substrate is meticulously cleaned using an organic cleaning station. This process encompasses sequential ultrasonic treatment with acetone for 10 min and isopropyl alcohol for 5 min, subsequently rinsed with deionized water and dried using a nitrogen gun to attain a pristine substrate surface. The spin-coating process is conducted on an HMDS/spin-coating stage, incorporating a pretreatment step of 10 min of HMDS treatment at 120 °C. Positive photoresist AZ6130 is utilized in conjunction with a spin-coating program, which starts with low-speed rotation at 600 rad/min for 5 s, followed by high-speed rotation at 4000 rad/min for 30 s. The post-bake conditions are set at 100 °C for 2 min. Lithography is executed using an MA6 lithography system with an exposure time of 2.3 s, followed by development using the 3038 developer (2.38% TMAH) for 45 s and a hardening treatment at 100 °C for 3 min.

During BDD patterning (channel length of 100 μm, line width of 10 μm), plasma etching is first performed at an ion energy of 400 eV, utilizing an ICP180 system with gas flow rates of O_2 at 80 sccm and Ar at 5 sccm, set with an ICP power of 1000 W and RF power of 150 W. The etching duration is precisely 2 min and 30 s. Following the etching, another cleaning sequence is implemented, including acetone and isopropanol ultrasonic cleaning, deionized water rinse, and nitrogen drying. The EDS elemental characterization following BDD processing can be found in Supplementary Material (Fig. S3).

Metal electrode deposition was performed in an FHR system, where a Cr/Au bilayer was deposited with thicknesses of 20 nm and 200 nm, respectively, at a sputtering power of 0.5 kW. The photolithography and etching steps were then repeated with identical process parameters to delineate the metal pattern. The stripping and cleaning procedures are again executed using the organic cleaning station, involving ultrasonic cleaning and drying as previously described. Subsequently, annealing is carried out

Table 1 Oligonucleotide DNA sequences

Type	Sequence of 21-mer DNA oligonucleotides
Probe DNA oligonucleotides	COOH-5′-CCAGCCCAAAATCTGTGATCT-3'
Complementary target	3′-GGTCGGGTTTTAGACACTAGA-5'
2-mer mismatched target	3′-GGTCGGGTTTTAGACACTACT-5'
4-mer mismatched target	3′-GGTCGGGTTAAAGACACTACT-5'
8-mer mismatched target	3′-GCACCCGTTAAAGACACGACT-5'

via a rapid annealing furnace, maintained at 420 °C for 3 min to establish ohmic contact between the electrodes. The microscopic images of the metal electrodes throughout the manufacturing process can be found in Supplementary Material (Fig. S4).

A 500 nm SiO_2 film is grown at 350 °C via a PECVD system under specific gas conditions of SiH_4 at 4 sccm and N_2O at 710 sccm. The spin-coating and photolithography process parameters are repeated as detailed in the previous step to define the SiO_2 layer pattern, exposing the electrode and sensing regions. SiO_2 etching is executed using an RIE system under gas conditions of SF_6 at 5.5 sccm, CHF_3 at 31 sccm, He at 150 sccm, at a pressure of 1850 mtorr, and power of 200 W (forward/average). The final stripping and cleaning are performed on an organic cleaning workstation, employing acetone ultrasonic cleaning for 10 min, followed by isopropanol ultrasonic cleaning for 5 min to complete sample preparation, where the microscopic images of the bonding wires are available in Supplementary Material (Fig. S5).

Device encapsulation is achieved through the application of an epoxy resin coating, which serves to protect the electrodes from solution interference in solution detection environments, while ensuring a single-channel parallel detection mode across all three sensing regions.

Mutant DNA detection

This study utilized APTES (3-aminopropyltriethoxysilane) for surface modification, employing silane as a linker molecule to immobilize DNA probe molecules onto the partially oxygen-terminated surface of the diamond sensing region. The oligonucleotide sequences purchased from Shanghai Bioscience Co., Ltd. are detailed in Table 1. The DNA target sequence was extracted from exon 21 of the epidermal growth factor receptor (EGFR), which serves as a biomarker for non-small cell lung cancer (NSCLC). Notably, mutations in exon 21 (L858R) account for approximately 40% of EGFR mutations in patients, facilitating the early detection of NSCLC via L858R screening.

The modification of DNA probes and the hybridization process can be categorized into the following steps. Initially, an oxygen plasma treatment is conducted by placing the device into an oxygen plasma de-coating machine. The parameters selected include 70 W power, −100 kPa pressure, and a treatment duration of 90 s, aimed at removing organic contamination from the device surface and enhancing hydroxyl content. Following this, an amination reaction is performed by immersing the sensing region of the device in a 2% APTES solution and incubating it at room temperature for 1 h. The device is then washed with anhydrous ethanol and subjected to heating on a hot plate at 120 °C for 5 min to eliminate excess ethanol and promote the curing of amino groups.

To activate the amino groups, the sensing region is immersed in a 1:1 mixture of 0.1 M NHS and 0.2 M EDC and incubated at room temperature for 1 h. Subsequently, the device is washed with deionized water and dried using nitrogen gas.

For DNA probe modification, the device sensing region is immersed in a 10 nM DNA probe solution diluted in 3× SSC buffer and incubated at room temperature for 4 h. Following this incubation, the device is washed first with 10 mM PBS buffer, then with deionized water, and dried with nitrogen gas. In the final DNA hybridization step, the device sensing region is immersed in a 10 nM DNA target solution diluted in 3× SSC buffer and incubated at room temperature for 1 h. In post-incubation, the device undergoes washing with 10 mM PBS buffer for 7 min to minimize non-specific binding, followed by rinsing with deionized water and drying with nitrogen gas. All detection steps were performed at room temperature (25 °C). The model of the testing instrument is provided in the Supplementary Material (Fig. S6).

Acknowledgements
This research was funded by General Program (52175388) funded by the National Natural Science Foundation of China.

Author details
[1]School of Electro-Mechanical Engineering, Guangdong University of Technology, Guangzhou, China. [2]Guangdong Provincial Key Laboratory of Minimally Invasive Surgical Instruments and Manufacturing Technology, Guangdong University of Technology, Guangzhou, China. [3]State Key Laboratory of High-Performance Tools, Guangdong University of Technology, Guangzhou, China. [4]Smart Medical Innovation Technology Center, Guangdong University of Technology, Guangzhou, China

Author contributions
Z.S.Y. conceived the idea, analyzed data, conducted the experiments and modified the paper; Z.L.L., Y.Z., and Y.S.C. conducted the experiments, analyzed data, and wrote the paper; Z.L.L. conducted simulation analysis; C.Y.W. provided scientific suggestions for the article.

Competing interests
The authors declare no competing interests.

Supplementary information The online version contains supplementary material available at https://doi.org/10.1038/s41378-026-01184-6.

Received: 10 December 2025 Revised: 1 January 2026 Accepted: 10 January 2026
Published online: 10 March 2026

References

1. Antonarakis, S. E. & Beckmann, J. S. Mendelian disorders deserve more attention. *Nat. Rev. Genet.* **7**, 277–282 (2006).
2. Kunkel, T. A. & Erie, D. A. DNA mismatch repair*. *Annu. Rev. Biochem.* **74**, 681–710 (2005).
3. Rossetti, G. et al. The structural impact of DNA mismatches. *Nucleic Acids Res.* **43**, 4309–4321 (2015).
4. Jorde, L. B. & Wooding, S. P. Genetic variation, classification and 'race'. *Nat. Genet.* **36**, S28–S33 (2004).
5. Jiang, T. et al. Toripalimab plus chemotherapy as second-line treatment in previously EGFR-TKI treated patients with EGFR-mutant-advanced NSCLC: a multicenter phase-II trial. *Signal Transduct. Target. Ther.* **6**, 355 (2021).
6. Ming, T. et al. Advancements in biosensors for point-of-care testing of nucleic acid. *Crit. Rev. Anal. Chem.* **55**, 1523–1538 (2025).
7. Hsu, I. C., Yang, Q., Kahng, M. W. & Xu, J. F. Detection of DNA point mutations with DNA mismatch repair enzymes. *Carcinogenesis* **15**, 1657–1662 (1994).
8. Goel, A., Nagasaka, T., Hamelin, R. & Boland, C. R. An optimized pentaplex PCR for detecting DNA mismatch repair-deficient colorectal cancers. *PLOS One* **5**, e9393 (2010).
9. Dincer, C. et al. Disposable sensors in diagnostics, food, and environmental monitoring. *Adv. Mater.* **31**, 1806739 (2019).
10. Wang, Y., Zhao, Y., Bollas, A., Wang, Y. & Au, K. F. Nanopore sequencing technology, bioinformatics and applications. *Nat. Biotechnol.* **39**, 1348–1365 (2021).
11. Crossley, B. M. et al. Guidelines for Sanger sequencing and molecular assay monitoring. *J. Vet. Diagn. Invest.* **32**, 767–775 (2020).
12. Fleige, S. & Pfaffl, M. W. RNA integrity and the effect on the real-time qRT-PCR performance. *Mol. Aspects Med.* **27**, 126–139 (2006).
13. Deepa, C., Rajeshkumar, L. & Ramesh, M. Preparation, synthesis, properties and characterization of graphene-based 2D nano-materials for biosensors and bioelectronics. *J. Mater. Res. Technol.* **19**, 2657–2694 (2022).
14. Lubin, A. A. & Plaxco, K. W. Folding-based electrochemical biosensors: the case for responsive nucleic acid architectures. *Acc. Chem. Res.* **43**, 496–505 (2010).
15. Ashley, K. Developments in electrochemical sensors for occupational and environmental health applications. *J. Hazard. Mater.* **102**, 1–12 (2003).
16. Vu, C.-A., Chen, W.-Y., Vu, C.-A. & Chen, W.-Y. Field-effect transistor biosensors for biomedical applications: recent advances and future prospects. *Sensors* **19**, 4214 (2019).
17. Hwang, M. T. et al. Highly specific SNP detection using 2D graphene electronics and DNA strand displacement. *Proc. Natl. Acad. Sci. USA* **113**, 7088–7093 (2016).
18. Meng, Q. et al. Overcoming Debye screening effect in field-effect transistors for enhanced biomarker detection sensitivity. *Nanoscale* **16**, 20864–20884 (2024).
19. Cao, S. et al. ISFET-based sensors for (bio)chemical applications: a review. *Electrochem. Sci. Adv.* **3**, e2100207 (2023).
20. Li, H. et al. Application of silicon nanowire field effect transistor (SiNW-FET) biosensor with high sensitivity. *Sensors* **23**, 6808 (2023).
21. Zhang, Y. et al. Interface-engineered field-effect transistor electronic devices for biosensing. *Adv. Mater.* **37**, 2306252 (2025).
22. Xie, M. et al. Biocompatible surface functionalization architecture for a diamond quantum sensor. *Proc. Natl. Acad. Sci. USA* **119**, e2114186119 (2022).
23. McCreery, R. L. Advanced carbon electrode materials for molecular electrochemistry. *Chem. Rev.* **108**, 2646–2687 (2008).
24. Ostojić, J., Stanković, D., Manojlović, D., Metelka, R. & Stanković, V. Theophylline electrochemical sensing in pharmaceutical drugs using disposable boron-doped diamond thin film electrodes. *Funct. Diam.* **5**, 2579320 (2025).
25. Tryk, D. A., Tachibana, H., Inoue, H. & Fujishima, A. Boron-doped diamond electrodes: the role of surface termination in the oxidation of dopamine and ascorbic acid. *Diam. Relat. Mater.* **16**, 881–887 (2007).
26. Fischer, M., Maity, S., Kuntumalla, M. K., Gani, G. & Hoffman, A. Subsurface nitrogen bonding, thermal stability, and retention of 200 eV N2+ implanted polycrystalline diamond studied by in situ X-ray photoelectron spectroscopy. *Appl. Surf. Sci.* **657**, 159740 (2024).
27. Wu, K. et al. Nanoscale detection and real-time monitoring of free radicals in a single living cell under the stimulation of targeting moieties using a nano-diamond quantum sensor. *Funct. Diam.* **4**, 2336524 (2024).
28. Zhang, Q. et al. Optimization of diamond sensor for trace detection of SARS-CoV-2 N-protein using Au nanoparticles. *Appl. Phys. Lett.* **123**, 083702 (2023).
29. Li, M. et al. Recent advances in diamond MOSFETs with normally off characteristics. *Funct. Diam.* **4**, 2357654 (2024).
30. Song, K.-S. et al. Label-free DNA sensors using ultrasensitive diamond field-effect transistors in solution. *Phys. Rev. E* **74**, 041919 (2006).
31. Sasaki, Y. & Kawarada, H. Low drift and small hysteresis characteristics of diamond electrolyte-solution-gate FET. *J. Phys. Appl. Phys.* **43**, 374020 (2010).
32. Kawarada, H., Araki, Y., Sakai, T., Ogawa, T. & Umezawa, H. Electrolyte-solution-gate FETs using diamond surface for biocompatible ion sensors. *Phys. Status Solidi A* **185**, 79–83 (2001).
33. Shintani, Y. et al. Polycrystalline boron-doped diamond with an oxygen-terminated surface channel as an electrolyte-solution-gate field-effect transistor for pH sensing. *Electrochimica Acta* **212**, 10–15 (2016).
34. Notsu, H., Yagi, I., Tatsuma, T., Tryk, D. A. & Fujishima, A. Surface carbonyl groups on oxidized diamond electrodes. *J. Electroanal. Chem.* **492**, 31–37 (2000).
35. Iniesta, J., Michaud, P. A., Panizza, M. & Comninellis, C. H. Electrochemical oxidation of 3-methylpyridine at a boron-doped diamond electrode: application to electroorganic synthesis and wastewater treatment. *Electrochem. Commun.* **3**, 346–351 (2001).
36. Denisenko, A., Jamornmarn, G., El-Hajj, H. & Kohn, E. pH sensor on O-terminated diamond using boron-doped channel. *Diam. Relat. Mater.* **16**, 905–910 (2007).
37. Dipalo, M., Pietzka, C., Denisenko, A., El-Hajj, H. & Kohn, E. O-terminated nano-diamond ISFET for applications in harsh environment. *Diam. Relat. Mater.* **17**, 1241–1247 (2008).
38. Edgington, R. et al. Boron δ-doped (1 1 1) diamond solution gate field effect transistors. *Biosens. Bioelectron.* **33**, 152–157 (2012).
39. Švorc, Ľ, Stanković, D. M. & Kalcher, K. Boron-doped diamond electrochemical sensor for sensitive determination of nicotine in tobacco products and anti-smoking pharmaceuticals. *Diam. Relat. Mater.* **42**, 1–7 (2014).
40. Hideshima, S. et al. Attomolar detection of influenza A virus hemagglutinin human H1 and Avian H5 using glycan-blotted field effect transistor biosensor. *Anal. Chem.* **85**, 5641–5644 (2013).
41. Nebel, C. E. et al. Diamond nano-wires, a new approach towards next generation electrochemical gene sensor platforms. *Diam. Relat. Mater.* **18**, 910–917 (2009).
42. Hazdra, P. et al. Low-resistance ohmic contacts on boron-doped {113} oriented homoepitaxial diamond layers. *Diam. Relat. Mater.* **121**, 108797 (2022).
43. Valappil, S. M. et al. Nanocarbon ohmic electrodes fabricated by coaxial arc plasma deposition for phosphorus-doped diamond electronics application. *AIP Adv* **12**, 085007 (2022).
44. Liu, D.-Y. et al. Effect of oxygen on regulation of properties of moderately boron-doped diamond films. *Chin. Phys. B* **31**, 128104 (2022).
45. Liu, J., Teraji, T., Bo, D. & Koide, Y. High output current boron-doped diamond metal-semiconductor field-effect transistors. *IEEE Electron Device Lett.* **40**, 1748–1751 (2019).
46. Kim, D.-S. et al. An FET-type charge sensor for highly sensitive detection of DNA sequence. *Biosens. Bioelectron.* **20**, 69–74 (2004).
47. Wang, Y. et al. A multiplexed electrochemical quantitative polymerase chain reaction platform for single-base mutation analysis. *Biosens. Bioelectron.* **214**, 114496 (2022).
48. Napoli, C. et al. Electronic detection of DNA hybridization by coupling organic field-effect transistor-based sensors and hairpin-shaped probes. *Sensors* **18**, 990 (2018).